Article

Detection of the infrared aurora at Uranus with Keck-NIRSPEC

Check for updates

Emma M. Thomas [1] ✉, **Henrik Melin** [1], **Tom S. Stallard** [2], **Mohammad N. Chowdhury** [1], **Ruoyan Wang** [1], **Katie Knowles** [2] & **Steve Miller**[3]

Near-infrared (NIR)-wavelength observations of Uranus have been unable to locate any infrared aurorae, despite many attempts to do so since the 1990s. While at Jupiter and Saturn, NIR investigations have redefined our understanding of magnetosphere–ionosphere–thermosphere coupling, the lack of NIR auroral detection at Uranus means that we have lacked a window through which to study these processes at Uranus. Here we present NIR Uranian observations with the Keck II telescope taken on the 5 September 2006 and detect enhanced H_3^+ emissions. Analysing temperatures and column densities, we identify an 88% increase in localized H_3^+ column density, with no significant temperature increases, consistent with auroral activity generating increased ionization. By comparing these structures against the Q_3^{mp} magnetic-field model and the Voyager 2 ultraviolet observations, we suggest that these regions make up sections of the northern aurora.

One of the most unusual aspects of Uranus is its magnetic field, off centred by a third of the planet's radius and tilted 59° from the planet's rotational axis[1]. With the planetary rotational axis also tilted by 98°, we are presented with a truly distinctive magnetosphere. The only flyby of the planet was made by Voyager II in 1986, where the data presented more questions than answers. Aurorae, presumably created by inter-actions between Uranus's magnetosphere and ionosphere, were first simultaneously detected by several instruments onboard Voyager II. Both radio (UKR) and ultraviolet (UV) emissions have shown auroral morphologies that are very different from those seen at Jupiter and Saturn and provide the foundation for auroral emission comparisons[2–4]. Investigations into Uranus's aurora have continued with the Hubble Space Telescope (HST)[5–8]. In these studies, 15 UV auroral emissions were identified: 9 southern aurora and 6 northern aurora emissions, largely consistent with pulsed cusp aurorae and observed to emit conjugately. In these previous investigations, the solar-wind conditions were found to greatly affect the Uranian aurorae, where Voyager II revealed a cor-relation between active solar-wind periods and UKR activity[9], with HST data showing positive detections (~25%) of UV auroral emissions that coincided with modelled peaks in solar-wind activity[5–8]. It is noted

that one UKR component (known as n-smooth) observed by ref. 10, originates from close to the magnetic equator at 2–3 R_U and was hence not considered auroral.

NIR emissions from H_3^+ (a molecular ion) have been fundamental in developing our understanding of the aurorae at Jupiter and Sat-urn[11–21]. H_3^+ was first discovered at Uranus in 1992 (ref. 22), and has been frequently analysed to characterize the ionosphere and understand seasonal and temporal changes therein. For 30 years, a continuous effort was made to document an infrared aurorae at Uranus[14,23–26]. In ref. 23, a 20% variation in H_3^+ emissions was tentatively attributed to auroral processes but due to the low signal-to-noise ratio, it could not be confirmed whether these increases were auroral. In ref. 26, a local-ized H_3^+ emission peak was observed on the dawnside limb of Uranus. Its location aligned with the southern aurorae latitudes; however, owing to time constraints, the feature could not be tracked and remains unconfirmed. From here on, when discussing the geometry of Uranus, we refer to the Uranian longitude coordinate system (ULS) presented by ref. 1. In addition, the exact longitude of Uranus during observations is unknown owing to the ±0.01 h rotational period uncertainty; hence, the longitude at Uranus is completely lost in ~3.4 Earth years.

[1]School of Physics and Astronomy, University of Leicester, Leicester, UK. [2]Department of Mathematics, Physics and Electrical Engineering, Northumbria University, Newcastle upon Tyne, UK. [3]Department of Physics and Astronomy, University College London, London, UK. ✉e-mail: emt18@leicester.ac.uk
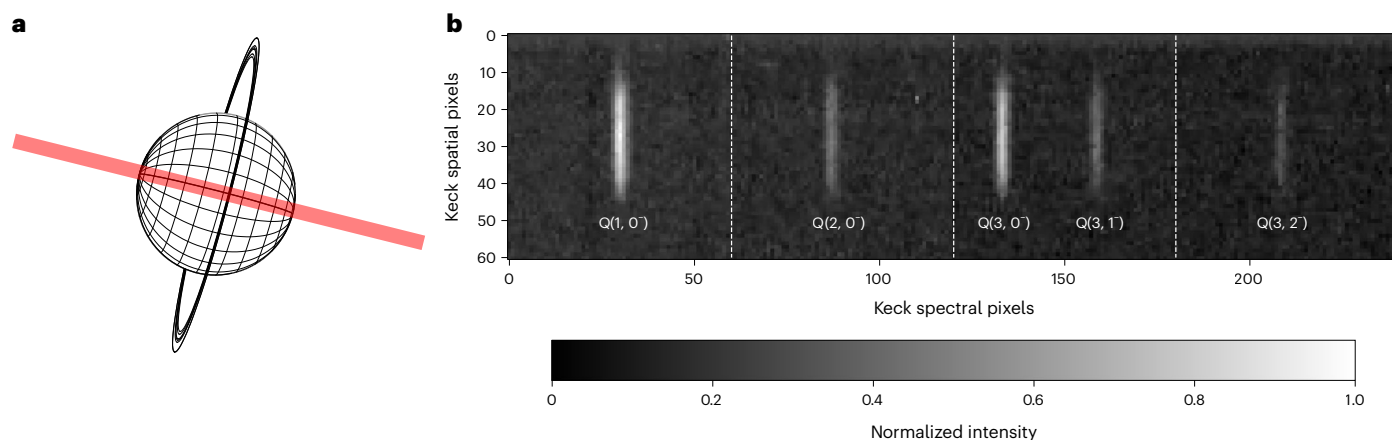
a

b

Fig. 1 | Observational set-up and averaged spectrum of Uranus as observed by Keck-NIRSPEC. a, The geometry of Uranus as was observed by KECK II SCAM (Slit-viewing camera) and NIRSPEC in September 2006. The orientation of the spectrometer slit on the disk of Uranus is shown in red, which aligns with the planet's rotational poles. **b**, An averaged spectra obtained by KECK II NIRSPEC between 3.4 μm and 4.0 μm, including annotations for Q(1,0⁻), Q(2,0⁻), Q(3,0⁻), Q(3,1⁻) and Q(3,2⁻) emission lines, which can be found at 3.9530 μm, 3.9708 μm, 3.9860 μm, 3.9865 μm and 3.9946 μm, respectively. Panel **a** made in part with Uranus Viewer 3.1, Ring-Moon Systems Node (https://pds-rings.seti.org/tools/viewer3_ura.shtml).

In this Article, we present high-resolution IR emissions at Uranus obtained over ~6 h in late 2006. We observe enhanced emissions that appear close to latitudes of the UV northern aurora (delineated by ref. [4]). To confirm whether these emissions are auroral, the spectra were analysed for temperature, column density and total emissions to identify whether enhancements were thermally driven or created by an ion population increase.

Uranus observations were taken with the Keck II telescope on the 5 September 2006, from 07:26 to 13:24 UT, close to the planet's equinox in 2007, using the NIRSPEC (Near-infrared Spectrograph) instrument[27] with a KL atmospheric window filter. A 0.288 × 24 arcsec slit was aligned with the plant's rotational axis (shown in Fig. 1a). Spectra were gathered between 3.5 μm and 4.1 μm where the fundamental Q-branch of H_3^+ emissions lies (shown in Fig. 1b; raw image in Extended Data Fig. 1). This triatomic hydrogen ion is a major constituent of Uranus's ionosphere and planets whose upper atmosphere is dominated by molecular and ionic hydrogen[28]. A total of 218 spectra were taken over an ~6 h period with an integration time of ~30 s. These were co-added into 13 datasets to enhance the signal-to-noise ratio (total integration time per set was ~27 min). To increase the signal-to-noise ratio further, spatial pixels along the slit were grouped every 0.32 arcsecs (full details in the Methods). The exact longitude of Uranus has been completely lost; therefore, an arbitrary longitude has been selected for these results. Astronomical seeing on the night averaged at 0.44 arcsec, which is equivalent to a blur of 14° latitude and 12° longitude. During the observation, Uranus rotated by ~180° and hence our final mapping spans an area up to ~180° longitude. Unfortunately, a lapse in guiding between 10:52 UT and 11:31 UT resulted in the loss of 2 longitudinal data bins, leaving a gap in the middle of our scans. Finally, results presented here are not corrected for line of sight (LOS) (for example, see ref. [16]) and hence we expect infrared emissions to be enhanced near the planet's limb. At Jupiter and Saturn, auroral emissions are LOS enhanced; however, Uranus's solar extreme ultraviolet (EUV)-generated ionosphere is darker at the limbs[7], and, so, without a detailed understanding of the ionospheric brightening source, it is not possible to correct. However, as much of the enhanced emissions are away from the limbs, we expect minimal change in the location of emissions peaks after corrections.

To calculate the H_3^+ intensities, temperatures, column densities and total H_3^+ emission for the upper atmosphere of Uranus, this study focuses on five quasi-thermalized ro-vibrational emission lines of H_3^+, Q(1,0⁻), Q(2,0⁻), Q(3,0⁻), Q(3,1⁻) and Q(3,2⁻); these physical parameters were calculated from a full spectrum best fit, as described in Methods.

The final fitted spectra provide intensity values that are then mapped across Uranus as is shown with the Q(1,0⁻) emission line (with the highest signal-to-noise ratio; Fig. 2a), H_3^+ total emission (Fig. 2b), temperatures (Fig. 2c) and H_3^+ column density (Fig. 2d). The respective error maps are shown in Extended Data Fig. 2a–d.

In Fig. 2a,b, the H_3^+ emission intensity varies with local time. To confirm the source of these enhancements, we define three regions of interest that are algorithmically distinct: the 'enhanced' region where the emissions are brighter than the mean plus one standard deviation (shown in solid black lines but not shaded); the 'dim' region where emissions are below the mean emission (shaded with dots); and the 'intermediate' region where emissions are brighter than the mean, but within a standard deviation of that mean (shaded by diagonal lines). The means and standard deviations for Fig. 2a,b,d presented in Table 1 are the result of subtracting each pixel by its uncertainty (seen in Extended Data Fig. 2). The resulting datasets are hence minimized, meaning pixels in the enhanced region are statistically significant.

In Fig. 2a, the enhanced regions show intriguing structures, the first, which is smaller, between 26° S and 59° S and from 18° to 28° longitude (E1). The second area extends between 15° N and 75 °N from 100° and 143° longitude with two smaller emission spots between 10° N and 0° and between 10° S and 20° S over a 108° to 117° longitude range, which we refer to as E2. Table 1 summarizes the mean values of Q(1,0⁻) intensities, along with mean values for temperature, column density and total H_3^+ emission. Comparing the dim region's mean Q(1,0⁻) intensity (0.472 ± 0.086 μW m⁻² sr⁻¹) with that of the enhanced region (0.723 ± 0.010 μW m⁻² sr⁻¹ and 0.716 ± 0.009 μW m⁻² sr⁻¹), we find a 27% to 90% enhancement.

Figure 2b shows the total H_3^+ emission, which is the combined intensity from all H_3^+ emission lines in this investigation. We find the two enhanced regions average at 6.155 ± 0.681 μW m⁻² sr⁻¹ and 6.354 ± 0.616 μW m⁻² sr⁻¹ for E1 and E2, respectively, while the dim region emits at a lower average of 3.212 ± 1.235 μW m⁻² sr⁻¹, hence an 18%, up to 353% increase at both E1 and E2. This large range in emission enhancement is most likely from the high uncertainty in column density, which affects the error propagation when calculating the total emission. We, however, conclude that our division of emissions of Uranus—whether the single Q(1,0⁻) line or total H_3^+ emission, into distinct enhancement related regions, is both robust and significant.

Comparing physical parameters between enhanced regions provides an understanding of how they are enhanced. The average temperature for the dataset is 585 ± 25 K, which aligns with previous
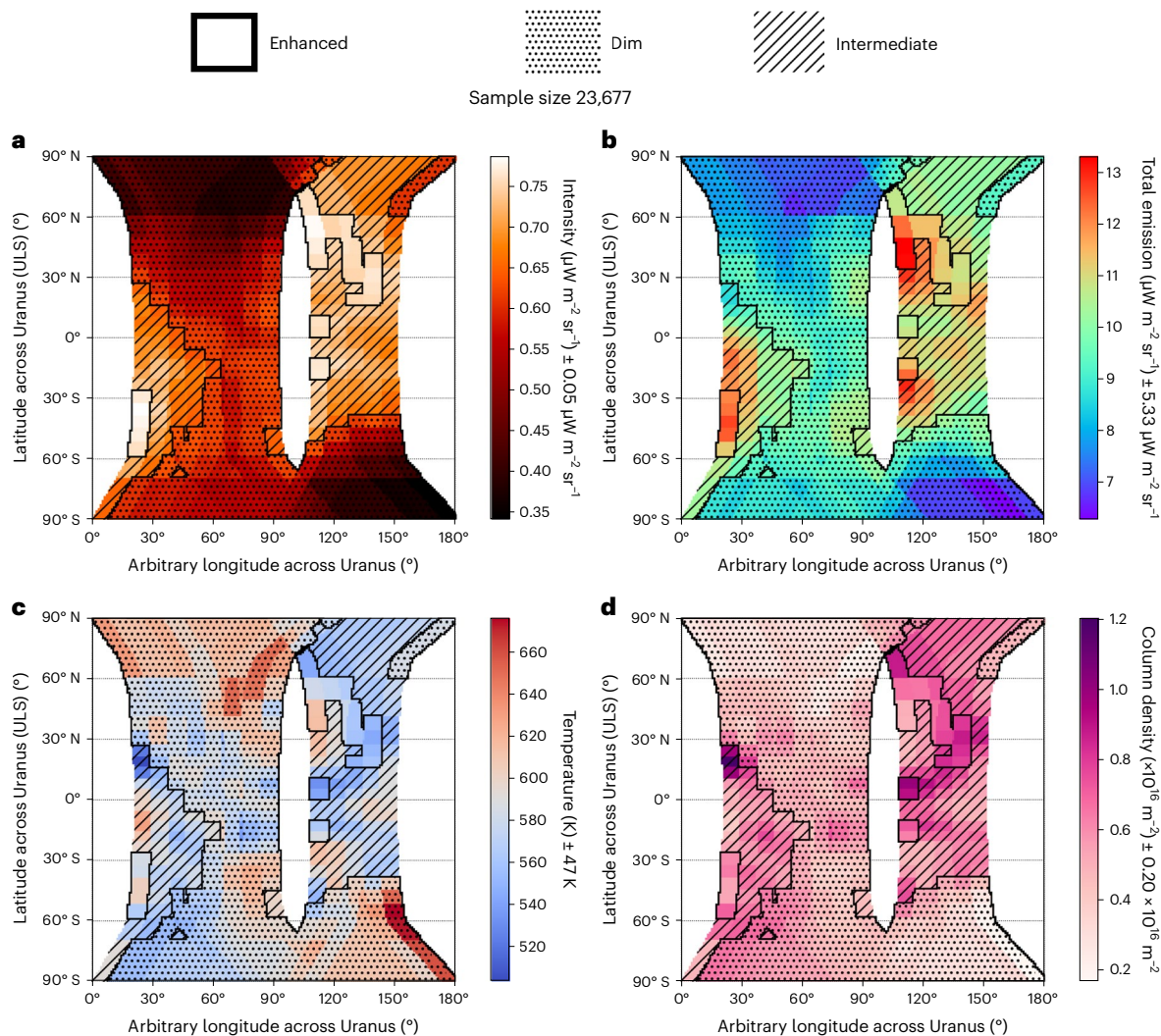
Fig. 2 | Infrared intensity, total emission, temperature and column-density mappings across Uranus on the night of observations. a, Measured H_3^+ $Q(1,0^-)$ intensity mapped across the upper atmosphere of Uranus against Uranian latitude and arbitrary longitude. **b**, Total H_3^+ emission calculated from the temperature and column density (explained in detailed in Methods). **c**, Estimated temperatures of the H_3^+ emissions from all five Q-branch lines. **d**, Estimated column densities of H_3^+ emissions from all five Q-branch lines. The latitude is planetocentric whereas the longitude is arbitrary due to the loss of the ULS since Voyager II. The solid black lines mark out the boundaries of E1 (left) and E2 (right). Within the boundaries, the enhanced regions are unshaded, the dim regions are shaded with dots and the intermediate regions are shaded with diagonal lines.

Table 1 | Means and standard deviations of the $Q(1,0^-)$ intensities, H_3^+ ion temperatures, ion column densities and total emission for the enhanced and dim regions

	Mean $Q(1,0^-)$ intensity ($\mu W\,m^{-2}\,sr^{-1}$)	Mean temperature (K)	Mean column density ($\times 10^{15}\,m^{-2}$)	Total H_3^+ emission ($\mu W\,m^{-2}\,sr^{-1}$)
Enhanced E1	0.723±0.010	585±14	4.017±0.457	6.155±0.887
Enhanced E2	0.716±0.009	564±22	5.113±0.826	6.354±0.616
Intermediate	0.650±0.032	572±19	4.134±0.761	5.354±0.664
Dim	0.472±0.086	593±24	2.432±0.901	3.212±1.235

temperature observations (ref. 25 for 2006 at 608 ± 12 K). The enhanced regions have a mean temperature of 585 ± 14 K and 564 ± 22 K for E1 and E2, respectively, with the dim region temperature at 593 ± 24 K, shown in Fig. 2c. While the enhanced regions appear cooler, there is overlap in temperature errors, so while we cannot conclude the emission is anticorrelated with temperature, thermal processes cannot explain the intensity enhancements.

Except at the planet's limbs, EUV ionization produces a uniform column ionization rate across the whole disk; however, enhancements

of column densities could be produced by enhanced particle precipitation, suggestive of auroral activity. Shown in Fig. 2d, we observe an average column-density difference of $2.133 \times 10^{15}\,m^{-2}$ at the enhanced regions ($4.017 \pm 0.457 \times 10^{15}\,m^{-2}$ and $5.113 \pm 0.826 \times 10^{15}\,m^{-2}$ at E1 and E2, respectively) compared with the dim region ($2.432 \pm 0.901 \times 10^{15}\,m^{-2}$). These densities, on average, are higher (about two to five times higher) than reported in ref. 25. Here a more through and complete data-reduction process was conducted over the whole night of observations rather than half the night, with densities presented in Table 1

aligning within the range of densities observed in previous investigations[25,26]. In contrast to the temperatures, the enhanced region's column density is on average 88% enhanced. Put simply, more emitters, rather than hotter emitters, is what is resulting in more emission.

There are several scenarios that could lead to a column-density enhancement at locations of increased H_3^+ emissions. One possibility is if the ion is produced evenly across the planetary disk, there is some mechanism by which it is transported from the dim region into the enhanced regions.

We do not consider meridional transport from the rotational poles to be substantial for two reasons: first, Uranus is a large, rapidly rotating planet where it is difficult to overcome the Coriolis forces; second, if there are equatorwards winds, we would expect to see a H_3^+ bulge evenly distributed at lower latitudes. There is nothing in our data to suggest polewards meridional transport.

Zonal winds on Uranus are generally between 0 and 250 m s^{-1}. A previous study[29] found electron densities between ~10^9 m^{-3} (Voyager egress) and ~10^{10}/10^{11} m^{-3} (Voyager ingress). Taking these figures together with the dissociative recombination coefficient of ~10^{-13} m^3 s^{-1} (ref. [30]) suggests a maximum half lifetime $\tau(H_3^+)$ of less than 10^4 s, and possibly as low as 100 s. Hence an individual H_3^+ ion could be transported ~2,000 km. This is less than the ~30,000 km at the equator to get from the centre of E2; although the distance from there to the centre of E1 is approximately half that value, it is still too far. Hence, we assume that the H_3^+ ions, their emissions and physical parameters are representative of locally produced features.

Another potential driver for the dim region's low column densities could be 'ring rain' as seen at Saturn[31]. Here, H_3^+ destruction is modulated by water molecules in the planet's rings travelling along the field lines into the planet's lower latitudes. Figure 3a combines Fig. 2a and the Q_3 model from ref. [32], which maps Uranus's magnetic field with dip angle contours, using contour steps of 20° dip angle (the angle made with the planet's horizontal plane by its magnetic-field lines). We expect the ring rain to affect only a narrow band of dip angles (mapping to the planet's rings, 1.6–2 R_U), where in Fig. 3a we observe the dim region over a large range of dip angles. Hence, quenching ring rain cannot explain the emissions we observe.

Two more magnetic-field models (Q_3^{mp} and AH$_5$; ref. [4]) have since been used at Uranus, replacing previous models with a more globally representative magnetopause image field and including UV auroral emissions from Voyager II, respectively. These models provide a strong fit to the southern aurora, but the northern aurora is poorly constrained as Voyager crossed magnetic-field lines that mapped close to the southern magnetic pole twice, once at a distance of 4.19 R_U, but only once at the north, at >20 R_U. In addition, the auroral morphology may have changed with solar-wind pressure or by changes in the preferred auroral acceleration region above the planet. Given this complexity, we focus solely on the Q_3 model.

As none of the previous processes can explain the NIR enhancement morphology, the most plausible explanation is that the density enhancements are driven by auroral production. In previous H_3^+ investigations at Jupiter and Saturn[11–13,15,17,18], we have observed the strongest infrared emission enhancements and column densities at the auroral regions, where particle precipitation results in significant ionization in the upper atmosphere. We find that the enhanced regions strongly suggest auroral production and so consider that we have partially mapped the northern infrared aurora.

To determine how the 2006 infrared emissions aligned with previous models, we have chosen to not add a longitude shift into our work due to the lack of known longitude (ULS) in 2006. Comparing Fig. 2a and the Q_3 model (Fig. 3a), we observe intensities between 60° and 80° dip angle at the same angle as where the auroral oval sits, although the approximate location of the auroral oval in the Q_3 model sits within the dim region (similar in location to Fig. 3b). Other enhanced regions with poor alignment (where the dip angle drops to 20°) may be due to more complex morphology within the surface magnetic-field structure, or

the effects of seeing (at least ~±12°) along with the low spatial resolution (~0.32 arcsec). We also note relatively weak emissions between 40° and 100° longitude. While most pixels in this region are 'dim', we highlight that these emissions remain brighter than the limbs. It may be that while the enhancement is not significant as the enhanced region, only the edges of the map represent the EUV ionized background H_3^+ density. This weaker central region could be driven by weaker auroral precipitation and hence further investigations are required.

In Fig. 3b, we compare the infrared emissions against the L-shell magnetic-field lines of the Q_3 model. Here the emissions observed in both E1 and E2 extend out past the optimal L5 shell, which is where the brightest UV emissions are observed by Voyager II and HST. Focusing on E1, between 30° S and 60° S and before 30° ULS longitude, we find no enhanced emissions align with the Q_3 L shells. These emissions are, however, located close to dayside O-source radio emissions[33], and are close to n-smooth radio emissions observed in ref. [10], where the authors suggested that these emissions arose from unusual particle distribution from particle absorption by the ε ring, which may act as a driver for these infrared extended emissions. We do, however, find a portion of E2 emissions fit within L shells of 3 and 5, where weak UV emissions in Fig. 3c are located (~<100 R).

Figure 3c compares Fig. 2a with UV auroral emissions from Voyager II in 1986. At Jupiter, UV and infrared aurora appear at similar latitudes[34,35]; however, at the auroral oval, ref. [36] found UV and infrared auroral features' brightness can vary independently of each other and hence are not co-located. We should then not expect the brightest NIR emissions to be co-located with the brightest UV emissions at Uranus. Further differences between infrared and UV emissions can also be explained by the ~15 min lifetime of H_3^+ (at Jupiter) smoothing out short-term (1–2 min) variability in UV emissions[37]. A similar effect may also occur at Uranus.

The enhanced H_3^+ emissions are broadly spaced in latitude compared with the brightest UV emission, where the strongest UV emissions occur north of E1 and only weaker UV emissions appear close to or at E2. This spreading of infrared emissions suggests that H_3^+ emissions occur more equatorwards (magnetic-field equator) than the UV emissions and appear anticorrelated in terms of longitude. Differences in emission region may result from changes in the auroral drivers, changes in the solar wind (as observed at Jupiter and Saturn[38]); or short-term variability associated with the local time. These might be via changing precipitation flux or precipitation energy. Equally, contrasts in apparent magnetic mapping of the two aurorae could originate from poor alignment of our arbitrary longitude. It is difficult to draw too many conclusions without re-discovering the rotational phase of Uranus.

This likely detection of H_3^+ aurora at Uranus has broader implications for Neptune, given the planet's similarities (similar unaligned and offset magnetic fields). Currently, we have not detected H_3^+ at Neptune[39], the cause suggested to be a cooler than expected upper atmosphere[28]. The presence of infrared aurora at Uranus suggests the potential for detecting aurora at Neptune, where past observations may have been taken during weak emission periods.

Confirming infrared aurora at Uranus directly assists in exoplanetary advancements as warm-ice-giant worlds make up a large fraction of the current population[40]. Auroral detections from exoplanets could provide upper atmospheric diagnostics. A detailed understanding of Uranus could advance exoplanet knowledge, helping the wider scientific community to understand their ionospheric compositions. Uranus also presents an ideal laboratory for observing conditions during magnetic-field reversal, as the magnetospheric axis consistently changes direction with respect to the solar wind, over a single Uranian day[41]. Current research requires analysis of volcanic rock at Earth or modelling to identify the effects of a reversal[42]. By undertaking consistent observations, we can identify changes in atmospheric processes, which extrapolated to Earth can enhance our modelling of misaligned magnetic fields.
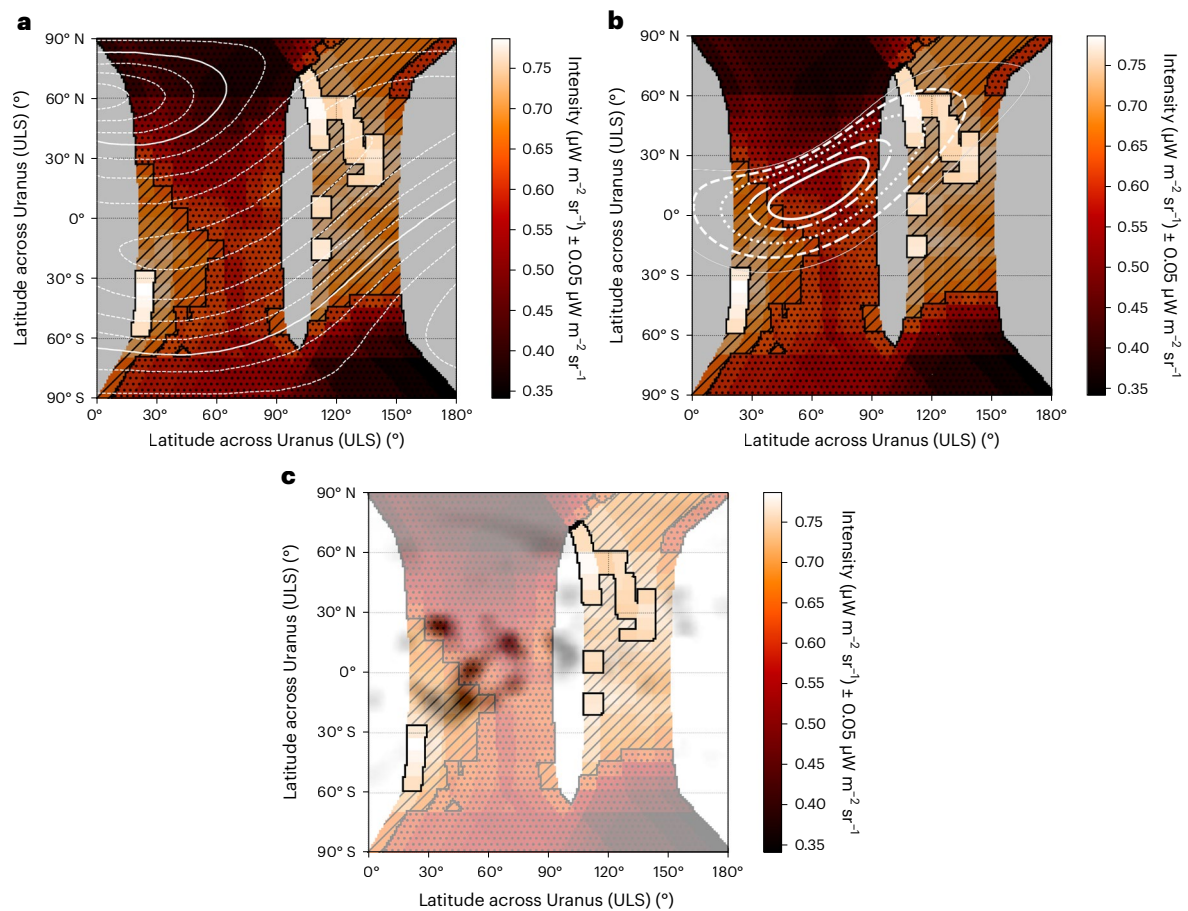
Fig. 3 | Infrared intensity mapping compared against previous Uranus magnetic-field models and UV emission data. a, $Q(1,0^-)$ mapped intensities with the Q_3 model[32] with contours representing the contours of 20° dip angles to the thick continuous white line, which is the magnetic-field equator. Here the ULS has been sourced and placed into our observations from the Q_3 model. The grey background colour represents the areas that were unobserved in these

observations. **b**, $Q(1,0^-)$ intensities (where only the enhanced region has been highlighted) mapped alongside the L shells of 2 (solid line), 3 (dashed), 5 (dotted), 10 (dot and dashed) and 20 (solid) of the Q_3 model. **c**, $Q(1,0^-)$ intensities (where only the enhanced region has been highlighted) mapped alongside the H_2 band emissions intensity map from ref. 4. To avoid obscuring the UV emissions, the dark grey background has been removed in this panel.

Methods

Introduction

This study uses 216 spectral images of H_3^+ emission taken on the 5 September 2006, the year before Uranus would reach equinox. These images were taken using the NIRSPEC instrument at the W.M. Keck II Observatory using a KL atmospheric window filter that covers the 3.3–5.0 µm range, reduced through the spectrometer grating to a 3.35–4.0 µm range to focus on the fundamental Q-branch emission of H_3^+ (which is known from previous investigations[25,26] to emit with a suitable signal-to-noise ratio). This wavelength range was used across all images including the reference star (HR 215143) and flat-field images.

Due to the slit length of 24″ across Uranus (which at the time subtended 3.7″ in the sky), we positioned the disk of the planet at two locations along the slit when taking images. The first frame (known as the A frame) centred the disk of Uranus in the top half of the slit, while the second frame (known as the B frame) centred the disk of Uranus in the bottom half of the slit. By carrying out this pattern, for the same sky position we would have alternating observations of Uranus's and Earth's atmospheric emission and the second with just Earth's atmospheric emission. The latter data could then be subtracted from the former to mitigate the effect of sky emissions.

Once all images were obtained, the data were then reduced using the Interactive Data Language (IDL)-based RedSpec data-reduction pipeline, which shifts data into straightened two-dimensional arrays by using the reference star images, as shown in the reference material.

To mitigate the effect of thermal currents or dead pixels on the detector, all reduced images were then calibrated using the flat and dark frames.

H_3^+ intensity calculations and mapping

Taking the images from the reference star frames (which at the time was closest to Uranus within the night sky and shown in Supplementary Fig. 1), the flux can be estimated by taking a Gaussian fit across the blackbody emission lines (similar to the Gaussian fit shown in Supplementary Fig. 2a,b). Once found, the measured flux observed can be compared against the known intensity of HR 215143, which is estimated using the work of ref. 43 with an α Lyrae (an A0) star. In this work, HR 215143 is a B7.5 V star, although the radius, mass and luminosity are of the same or similar magnitude to that of A0 (A0V) stars[44]; hence, we use the calculations of ref. 43 as a close representation for the expected flux of HR 215143. The expected temperature of HR 215143 is, however, at approximately 11,000 K instead of 10,000 K (as expected of A0 stars) as calculated from the work of ref. 45; this difference in temperature is included in the calculations described above.

This ratio can then be used to convert detector counts from images into a known intensity value, which was carried out across all images. These images were then grouped into 54 sets of data and aligned (in case Uranus had appeared to shift across the slit) by using a Python script that detected the disk of the planet by measuring the central position within the longest sequence of pixels with emission values 1 s.d. greater than the background emission and shifting data

by the required number of pixels so that individual spectra could be co-added.

When all the data had been correctly lined up, to enhance the signal-to-noise ratio, the data were binned into 13 temporal sets of data across ~6 h of observations. This was completed by the sequence in which A frames and B frames were taken, in an ABBA pattern where two added A frames are subtracted by two B frames and averaged. By averaging four datasets (over the previous 54 sets) at a time, it was possible to obtain a spectrum with sufficient signal-to-noise ratio to complete Gaussian fitting, as seen in Supplementary Data Fig. 2a,b. Originally Uranus was found to cover just under 23 pixels (22.9 pixels) across the detector, the limbs of which were found by code that searched each of the 13 temporal datasets for enhanced emission lines that extended for 22–23 pixels; from this the approximate middle of the disk could be deduced.

A further enhancement of the signal-to-noise ratio was required to minimize the error in intensity and so a 2 pixel weighted rolling average was chosen to enhance the signal strength. This would mean starting from the northern limb, the first and second pixels were averaged and assigned to the first mapped pixel, then the second and third pixels were averaged and assigned the second mapped pixel and so on. This resulted in a total of 22 pixels across Uranus, allowing identification of auroral or enhanced regions.

To find the observed intensity from all emission lines, the h3ppy Python package (a Python version of the C++ fitting procedure as detailed in ref. [35]) was used. This produces multiple Gaussian fits across a spectrum with a known range of wavelength, with intensities for each line varying with modelled temperature and column density. The calculations behind this are explained in detail in ref. [17]. It should be noted due to the changing LOS of the observer across Uranus's disk, the intensity will be enhanced at the limb of the planet due to the observer effectively viewing through more of the atmosphere. The background solar EUV when modelled at Uranus diminishes at the edges and with the majority of the data localized away from the limb, we have not adjusted for this effect. The errors in the intensity of $Q(1,0^-)$ were calculated by the errors in fitting a Gaussian curve with the observed emission line (errors predominantly arising from the height and width of the fit).

H_3^+ ro-vibrational temperature calculations
By applying a full spectra best fit across emission lines $Q(1,0^-)$, $Q(2,0^-)$, $Q(3,0^-)$, $Q(3,1^-)$ and $Q(3,2^-)$, the ro-vibrational temperatures can be calculated using ab initio Einstein A coefficients—physical parameters of H_3^+ spectra emission lines as detailed by ref. [46] and the upper energy levels as described by ref. [47]. This process is carried out with the h3ppy package (see Supplementary Fig. 3 for a visual representation of this fitting with an averaged spectrum from the 5 September) assuming a quasi-local thermodynamic equilibrium H_3^+ spectra fit[20].

H_3^+ column-density calculations
This data product was calculated by dividing the measured intensity from the observed emission lines by the theoretical emission per molecule for all the Q-branch emission lines mentioned in the temperature calculations, as described by ref. [24]. It should be noted due to the LOS of the observer across Uranus's disk, the column density will be enhanced at the limb of the planet due to the observer effectively viewing through the atmosphere twice. At present, these results have not been adjusted for this effect, as most of the data are localized away from the limb of the planet, but we estimate that, within the auroral regions discussed, this enhancement would be 14%.

H_3^+ total emission calculations
Using the calculations of ref. [46], the total emission can be calculated by the product of the number of ions by the temperature-dependent total emission per molecule (E^{mol}) while assuming local thermal equilibrium.

This requires both the column density and temperature over two or more emission lines), where temperature is used to calculate E^{mol}. It should be highlighted that due to temperatures staying between $500\,K \le T \ge 900\,K$, suitable coefficient values were selected to calculate E^{mol}.

References
1. Ness, F. N. et al. Magnetic fields at Uranus. *Science* **233**, 85–89 (1986).
2. Curtis, S. A., Desch, M. D. & Kaiser, M. L. The radiation belt origin of Uranus' nightside radio emission. *J. Geophys. Res. Space Phys.* **92**, 15199–15205 (1987).
3. Kaiser, M. L., Desch, M. D. & Curtis, S. A. The sources of Uranus' dominant nightside radio emissions. *J. Geophys. Res. Space Phys.* **92**, 15169–15176 (1987).
4. Herbert, F. Aurora and magnetic field of Uranus. *J. Geophys. Res.* **114**, A11206 (2009).
5. Lamy, L. et al. Earth-based detection of Uranus' aurorae. *Geophys. Res. Lett.* **39**, L07105 (2012).
6. Lamy, L. et al. The aurorae of Uranus past equinox. *J. Geophys. Res. Space Phys.* **122**, 3997–4008 (2017).
7. Lamy, L. et al. Analysis of HST, VLT and Gemini coordinated observations of Uranus late 2017: a multi-spectral search for auroral signatures. In *Proc. Société Francaise d'Astronomie et d'Astrophysique (SF2A)*, (eds Di Matteo, P. et al.) 237–240 (2018).
8. Lamy, L. Auroral emissions from Uranus and Neptune. *Phil. Trans. R. Soc. A* **378**, 20190481 (2020).
9. Desch, M. D., Kaiser, M. L. & Kurth, W. S. Impulsive solar wind-driven emission from Uranus. *J. Geophys. Res. Space Phys.* **94**, 5255–5263 (1989).
10. Kaiser, M. L., Desch, M. D. & Connerney, J. E. P. Radio emission from the magnetic equator of Uranus. *J. Geophys. Res. Space Phys.* **94**, 2399–2404 (1989).
11. Drossart, P. et al. Detection of H_3^+ on Jupiter. *Nature* **340**, 539–541 (1989).
12. Geballe, T. R., Jagod, M.-F. & Oka, T. Detection of H_3^+ infrared emission lines in Saturn. *Astrophys. J.* **408**, L109–L112 (1993).
13. Stallard, T. S. et al. Complex structure within Saturn's infrared aurora. *Nature* **456**, 214–217 (2008).
14. Stallard, T. S. et al. Temperature changes and energy inputs in giant planet atmospheres: what we are learning from H_3^+. *Phil. Trans. R. Soc. A* **370**, 5213–5224 (2012).
15. Stallard, T. S. et al. Local-time averages maps of H_3^+ emission, temperature and ion winds. *Phil. Trans. R. Soc. A* **377**, 20180405 (2019).

16. Johnson, R. E., Stallard, T. S., Melin, H., Nichols, J. D. & Cowley, S. W. H. Jupiter's polar ionospheric flows: high resolution mapping of spectral intensity and line-of-sight velocity of H_3^+ ions. *J. Geophys. Res.Space Phys.* **122**, 7599–7618 (2017).

17. Johnson, R. E. et al. Mapping H_3^+ temperatures in Jupiter's northern auroral ionosphere using VLT-CRIRES. *J. Geophys. Res. Space Phys.* **123**, 5990–6008 (2018).

18. Chowdhury, M. N., Stallard, T. S., Melin, H. & Johnson, R. E. Exploring key characteristics in saturn's infrared auroral emissions using VLT-CRIRES: H_3^+ intensities, ion line-of-sight velocities and rotational temperatures. *Geophys. Res. Lett.* **46**, 7137–7146 (2019).

19. Miller, S. et al. The role of H_3^+ in planetary atmospheres. *Phil. Trans. R. Soc. A* **358**, 2485–2502 (2000).

20. Miller, S., Stallard, T. & Smith, C. H_3^+: the driver of giant planet atmospheres. *Phil. Trans. R. Soc. Lond. A* **364**, 3121–3137 (2006).

21. Miller, S., Tennyson, J., Geballe, T. R. & Stallard, T. Thirty years of H_3^+ astronomy. *Rev. Mod. Phys.* **92**, 035003 (2020).

22. Trafton, L. M., Geballe, T. R., Miller, S., Tennyson, J. & Ballester, G. E. Detection of H_3^+ from Uranus. *Astrophys. J.* **405**, 761–766 (1993).

23. Lam, H. A. et al. Variation in the H_3^+ emission of Uranus. *Astrophys. J.* **474**, L73 (1997).

24. Trafton, L. M., Miller, S., Geballe, T. R., Tennyson, J. & Ballester, G. E. H_2 quadrupole and H_3^+ emission from Uranus: the Uranian thermosphere, ionosphere, and aurora. *Astrophys. J.* **524**, 1059 (1999).

25. Melin, H. et al. Seasonal variability in the ionosphere of Uranus. *Astrophys. J.* **729**, 134 (2011).

26. Melin, H. et al. The H_3^+ ionosphere of Uranus: decades-long cooling and local-time morphology. *Phil. Trans. R. Soc. A* **377**, 20180408 (2019).

27. McLean, I. S. et al. The design and development of NIRSPEC: a near-infrared echelle spectrograph for the Keck II telescope. *Proc. SPIE* **3354**, 566 (1998).

28. Moore, L., Moses, J. I., Melin, H., Stallard, T. S. & O'Donoghue, J. Atmospheric implications of the lack of H_3^+ detection at Neptune. *Phil. Trans. R. Soc. A* **378**, 20200100 (2020).

29. Lindal, G. F. et al. The atmosphere of Uranus: results of radio occultation measurements with Voyager 2. *J. Geophys. Res. Space Phys.* **92**, 14987–15001 (1987).

30. Larsson, M., McCall, B. J. & Orel, A. E. The dissociative recombination of H_3^+—a saga coming to an end? *Chem. Phys. Lett.* **462**, 145–151 (2008).

31. O'Donoghue, J. et al. The dominations of Saturn's low-latitude ionosphere by ring 'rain'. *Nature* **496**, 193–195 (2013).

32. Connerney, J. E. P., Acuña, M. H. & Ness, N. F. The magnetic field of Uranus. *J. Geophys. Res. Space Phys.* **92**, 15329–15336 (1987).

33. Desch, M. D. et al. Uranus as a radio source. In *Uranus* (eds. Bergstralh, J. et al.) Part VI - Magnetosphere, 894–925 (1991).

34. Clarke, J. T. et al. In *Jupiter: The Planet, Satellites and Magnetosphere* (eds. Bagenal, F. et al.) Ch. 26 (Cambridge Univ. Press, 2007).

35. Melin, H., Miller, S., Stallard, T., Smith, C. & Grodent, D. Estimated energy balance in the Jovian upper atmosphere during an auroral heating event. *Icarus* **181**, 256–265 (2006).

36. Radioti, A., Lystrup, M., Bonfond, B., Grodent, D. & Gérard, J.-C. Jupiter's aurora in ultraviolet and infrared: simultaneous observations with the Hubble Space Telescope and the NASA Infrared Telescope Facility. *J. Geophys. Res. Space Phys.* **118**, 2286–2295 (2013).

37. Stallard, T. S. et al. Stability within Jupiter's polar auroral 'swirl region' over moderate timescales. *Icarus* **268**, 145 (2016).

38. Clarke, J. T. et al. Response of Jupiter's and Saturn's auroral activity to the solar wind. *J. Geophys. Res. Space Phys.* **114**, (2009).

39. Melin, H. et al. The quest for H_3^+ at Neptune: deep burn observations with NASA IRTF iSHELL. *Mon. Not. R. Astron. Soc.* **474**, 3714–3719 (2018).

40. Wolfgang, A., Rogers, L. A. & Ford, E. B. Probabilistic mass–radius relationship for sub-Neptune-sized planets. *Astrophys. J.* **825**, 19–23 (2016).

41. Cowley, S. W. H. Response of Uranus's auroras to solar wind compressions at equinox. *J. Geophys. Res. Space Phys.* **118**, 2897–2902 (2013).

42. Glatzmaier, G. A. & Roberts, P. H. A three-dimensional convective dynamo solution with rotating and finitely conducting inner core and mantle. *Phys. Earth Planet. Inter.* **91**, 63–75 (1995).

43. Blackwell, D. E., Leggett, S. K., Petford, A. D., Mountain, C. M. & Selby, J. Absolute calibration of the infrared flux from Vega at 1.24, 2.20, 3.76 and 4.6 μm by comparison with a standard furnace. *Mon. Not. R. Astron. Soc.* **205**, 897–905 (1983).

44. Pecaut, M. J. & Mamajek, E. E. Intrinsic colors, temperatures, and bolometric corrections of pre-main-sequence stars. *Astrophys. J. Suppl. Ser.* **208**, 9 (2013).

45. Silaj, J., Jones, C. E., Sigut, T. A. A. & Tycner, C. The Hα profiles of Be shell stars. *Astrophys. J.* **795**, 82–84 (2014).

46. Neale, L., Miller, S. & Tennyson, J. Spectroscopic properties of the H_3^+ molecule: a new calculated line list. *Astrophys. J.* **464**, 516–520 (1996).

47. Miller, S. & Tennyson, J. Hot band transition frequencies and line strengths in H_3^+: first principles calculations. *J. Mol. Spectrosc.* **136**, 223–240 (1989).

Acknowledgements

Author contributions

E.M.T. performed data reduction and data analysis, and contributed to the writing and editing of the paper. H.M. was responsible for the data analysis with the use of h3ppy. T.S.S. contributed via data reduction and data analysis. M.N.C. was responsible for IDL to Python code conversion for two-dimensional mapping over a three-dimensional surface. K.K. and R.W. contributed to the discussion and editing of the paper. S.M. is the principal investigator for the observations of Uranus taken in 2006 and contributed to the paper via discussion and editing of the paper.

Competing interests

The authors declare no competing interests.

Additional information

**Extended data** is available for this paper at https://doi.org/10.1038/s41550-023-02096-5.

Publisher's note Springer Nature remains neutral with regard to jurisdictional claims in published maps and institutional affiliations.

Extended Data Fig. 1 | Averaged ABBA spectrum of Uranus observed between 3.9445 μm and 4.0044 μm by NIRSPEC on the 5th September 2006. The Q(1,0⁻) emission line can be observed at 3.9530 μm with the Q(2,0⁻), Q(3,0⁻), Q(3,1⁻) and Q(3,2⁻) emission lines at 3.9708, 3.9860, 3.9865 and 3.9946 μm respectively.
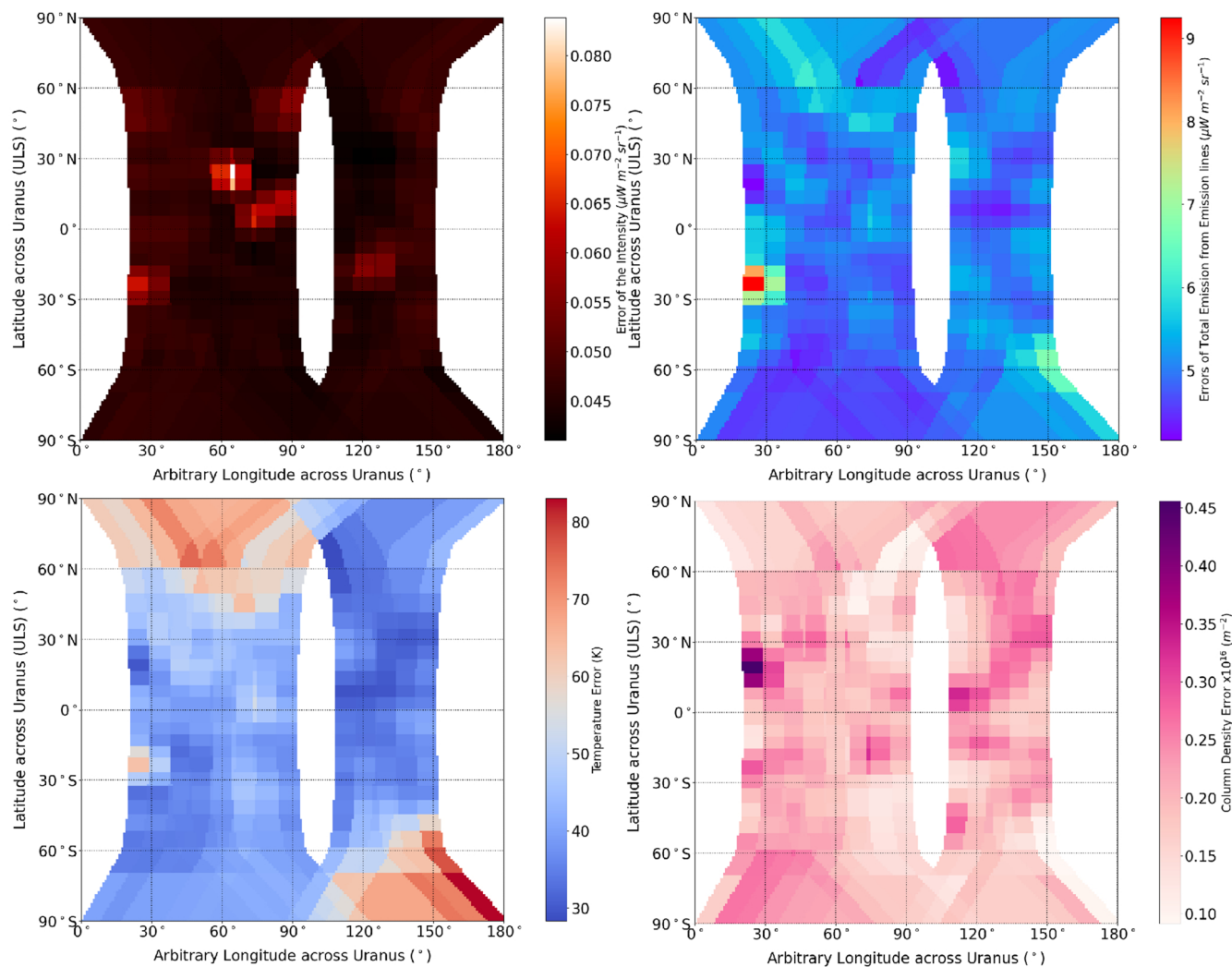
Extended Data Fig. 2 | a) Intensity errors calculated from the Q(1,0⁻) emission line, b) Total H$_3^+$ emission errors c) Temperature errors and d) Column Density errors across 180° longitude. Errors for the Intensity were calculated from the error in fitting the Gaussian with the emission line via the error in height and width propagated. Errors in Total Emission, Temperature and Column Density were calculated through h3ppy's fit of the emission spectra and following calculations.